

Dual-axes confocal reflectance microscope for distinguishing colonic neoplasia

Jonathan T. C. Liu

Stanford University
Ginzton Laboratory
Stanford, California 94305
and
School of Medicine
Stanford, California 94305

Michael J. Mandella

Stanford University
Ginzton Laboratory
Stanford, California 94305

Shai Friedland Roy Soetikno

Stanford University
School of Medicine
Stanford, California 94305

James M. Crawford

University of Florida
Department of Pathology
Gainesville, Florida 32610

Christopher H. Contag

Stanford University
School of Medicine
Stanford, California 94305

Gordon S. Kino

Stanford University
Ginzton Laboratory
Stanford, California 94305

Thomas D. Wang

Stanford University
School of Medicine
Stanford, California 94305

Abstract. A dual-axes confocal reflectance microscope has been developed that utilizes a narrowband laser at 1310 nm to achieve high axial resolution, image contrast, field of view, and tissue penetration for distinguishing among normal, hyperplastic, and dysplastic colonic mucosa *ex vivo*. Light is collected off-axis using a low numerical aperture objective to obtain vertical image sections, with 4- to 5- μm resolution, at tissue depths up to 610 μm . Post-objective scanning enables a large field of view ($610 \times 640 \mu\text{m}$), and balanced-heterodyne detection provides sensitivity to collect vertical sections at one frame per second. System optics are optimized to effectively reject out-of-focus scattered light without use of a low-coherence gate. This design is scalable to millimeter dimensions, and the results demonstrate the potential for a miniature instrument to detect precancerous tissues, and hence to perform *in vivo* histopathology. © 2006 Society of Photo-Optical Instrumentation Engineers. [DOI: 10.1117/1.2363363]

Keywords: laser scanning confocal microscopy; reflectance imaging; heterodyne detection; dysplasia; endoscopy; *in vivo* imaging.

Paper 05365RR received Dec. 5, 2005; revised manuscript received May 19, 2006; accepted for publication May 23, 2006; published online Oct. 24, 2006.

1 Background and Introduction

Confocal microscopes are used in bench top biological investigations to perform optical sectioning,¹ and can be used for *in vivo* imaging if the objectives and scanning mechanisms can be made sufficiently small. Over the past decade, numerous efforts have been made to miniaturize confocal microscopes.²⁻⁷ In order to achieve subcellular resolution with a conventional single-axis confocal microscope, a high numerical aperture (NA) is necessary, generally utilizing complex and bulky objective lenses for diffraction-limited focusing of beams over a wide field of view. Geometrically, a high

NA correlates to a short working distance for a given aperture size, thus limiting the depth at which subsurface imaging may be performed in tissue. Due to short working distances, scanning must be performed prior to the objective, which limits the field of view and introduces optical aberrations unless compensated for by the use of multiple lenses.⁴ Scaling down the optics unavoidably requires a sacrifice of resolution, field of view (FOV), and/or working distance (WD). In addition, the conventional single-axis confocal design is limited in its ability to effectively reject the large amounts of scattered light generated when imaging deeply in tissues (see Section 2).⁸

Address all correspondence to: Jonathan T.C. Liu, Ginzton Labs, Box N-123, 450 Via Palou, Stanford, CA 94305; E-mail: jonliu@stanford.edu

1083-3668/2006/11(5)/054019/10/\$22.00 © 2006 SPIE

In the United States, colorectal carcinoma is the second leading cause of death by cancer. Dysplasia is a precancerous condition that has a latency period of 5 to 10 years, where early detection is preventative. Colonic polyps are generally classified as adenomatous (dysplastic) or hyperplastic (benign). An endoscope-compatible confocal microscope that can distinguish among normal, hyperplastic, and dysplastic colonic mucosa may significantly improve the efficiency of colorectal cancer screening.

In order to distinguish histological differences in colonic mucosa, observation of glandular morphology with subcellular detail is needed. Thus, an axial and transverse resolution of at least $5 \mu\text{m}$ is required for resolving nuclear features, and an FOV and WD greater than $500 \mu\text{m}$ is needed to span the dimensions of the mucosa, which is the primary origin of epithelial neoplasia. The dual-axes confocal architecture uses low-NA lenses to achieve high-resolution imaging with a long WD.⁸⁻¹¹ Furthermore, the incident beams are on-axis to the low-NA lenses at all times, and scanned post-objectively. This configuration allows the design to be scaled down to millimeter dimensions, for endoscopic use, while preserving diffraction-limited optical quality and image resolution. Scanning can then be performed with a micro-mirror fabricated with MEMS technology.⁵

Over the past decade or so, an optical vertical sectioning technique, known as optical coherence tomography (OCT), has been developed for reflectance imaging in tissue.¹²⁻¹⁷ OCT, in its most basic form, uses an interferometer to analyze coherent light backscattered from a layer of tissue, by interfering it with light traveling along a reference path of nearly equal length. A low-coherence (broadband) light source, whose coherence length defines the axial resolution of the image, is used.

While OCT utilizes the coherence properties of light to produce optical sectioning, the confocal effect utilizes spatial filtering to achieve sectioning. Previously, we demonstrated a dual-axes microscope that utilized a broadband light source for the additional sectioning performance provided by a low-coherence gate. Here, we demonstrate that a narrowband light source may be used without a coherence gate, in a refined dual-axes prototype, to generate high-quality images in the colon. This results in greater simplicity of instrument design and possibly reduced cost. Furthermore, there is the potential to incorporate incoherent imaging modalities such as fluorescence for functional imaging of molecular biomarkers.^{18,19}

2 Theory

The point spread function for the dual-axes confocal architecture can be derived from diffraction theory, using the paraxial approximation, to calculate the response and resolution of the system. This theory takes into account the effect of finite apertures that result in truncated Gaussian beams, which is relevant to a fiber-optic-coupled instrument. First, from Fig. 1, the coordinate transformations of the illumination (x_i, y_i, z_i) and collection (x_c, y_c, z_c) beams in terms of the dual-axes coordinates (x_d, y_d, z_d) may be expressed as

$$x_i = x_d \cos \theta - z_d \sin \theta \quad x_c = x_d \cos \theta - z_d \sin \theta$$

$$y_i = y_d \quad y_c = y_d$$

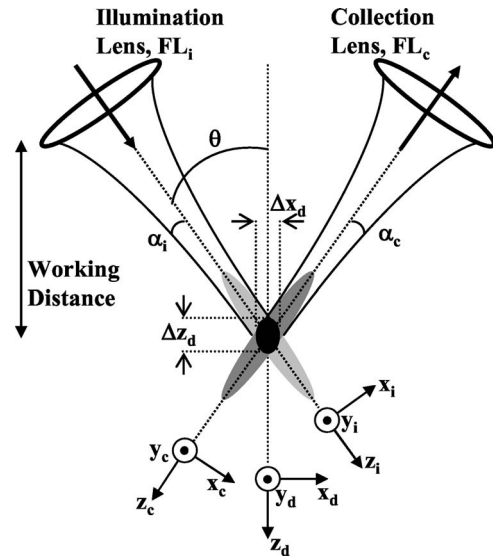


Fig. 1 Schematic diagram of the dual-axes design. The main lobe of the point spread function of the illumination beam (light-gray oval) at the focal point has a narrow transverse but a long axial dimension. The main lobe of the collection beam (dark-gray oval) is similar in shape. The intersecting region (black oval) is characterized by narrow transverse dimensions, Δx_d and Δy_d , and a reduced axial dimension, Δz_d .

$$z_i = x_d \sin \theta + z_d \cos \theta \quad z_c = -x_d \sin \theta + z_d \cos \theta. \quad (1)$$

In Fig. 1, α_i and α_c are the half-angles of the focused illumination and collection beams in the sample medium, defined by the radii of the focusing lenses, FL_i and FL_c , respectively. θ is the half-angle at which the beam axes intersect, also specified within the sample medium. A set of general dimensionless coordinates may be defined along the illumination and collection axes:²⁰

$$u_i = k_i n z_i \sin^2 \alpha_i \quad u_c = k_c n z_c \sin^2 \alpha_c$$

$$v_i = k_i n \sqrt{x_i^2 + y_i^2} \sin \alpha_i \quad v_c = k_c n \sqrt{x_c^2 + y_c^2} \sin \alpha_c, \quad (2)$$

where the illumination and collection wavenumbers are respectively defined as $k_i = 2\pi/\lambda_i$ and $k_c = 2\pi/\lambda_c$. λ_i and λ_c are the wavelengths of the illumination and collection beams in free space, respectively, and n is the sample's index of refraction. For the reflectance system described here, $\lambda_i = \lambda_c = 1.3 \mu\text{m}$.

The amplitude point spread function (PSF) is an expression that describes the spatial distribution of the electric field of the focused beams. The PSF of the illumination and collection beams are proportional to the integrals below:²⁰

$$U_i(v_i, u_i) \propto \int_0^1 W_i(\rho) J_0(\rho v_i) e^{-j u_i \rho^2 / 2} \rho d\rho, \quad (3)$$

$$U_c(v_c, u_c) \propto \int_0^1 W_c(\rho) J_0(\rho v_c) e^{-j u_c \rho^2 / 2} \rho d\rho, \quad (4)$$

where J_0 is the Bessel function of order zero, and ρ is a normalized radial distance variable at the lens aperture. The weighting function, $W(\rho)$, describes the truncation (apodization) of the beams. For uniform illumination, $W(\rho)=1$. For Gaussian illumination with the cut-off aperture located at the $1/e^2$ intensity fall-off point, the weighting function is $W(\rho) = e^{-\rho^2}$. In this system, the beams are truncated at the point where 99% of the Gaussian beam power is transmitted. For a Gaussian beam with a radius ($1/e^2$ intensity) given by w , an aperture with diameter πw passes approximately 99% of the beam's power.²¹ In this case, the weighting function is

$$W(\rho) = e^{-(\pi\rho/2)^2}. \quad (5)$$

For a single-axis confocal microscope, the illumination and collection PSFs at the focal plane ($u_i=u_c=0$), denoted by U_s , are identical as a function of the radial distance ρ , and with $v=knr \sin \alpha$, are

$$U_s(v) \propto \int_0^1 W_i(\rho) J_0(\rho v) \rho d\rho. \quad (6)$$

The detector output from a point reflector, V_d , is proportional to the power received, which is proportional to the square of the product of the overlapping point spread functions:

$$V_d = A |U_i U_c|^2, \quad (7)$$

where A is a constant.

For uniform illumination ($W=1$), the detector output V_s for a single-axis system is

$$V_s \propto \left(\frac{2J_1(v)}{v} \right)^4. \quad (8)$$

Similarly, since the depth of focus for a single beam, described within the third term (exponential term) in the integral product in Eqs. (3) and (4), is much larger than the transverse width of a single beam, that exponential term may be neglected to solve for the response of the dual-axes system near the focus, for uniform illumination:

$$V_d \propto \left(\frac{2J_1(v_i)}{v_i} \right)^2 \left(\frac{2J_1(v_c)}{v_c} \right)^2. \quad (9)$$

In a previous article,²² this expression was used with Eqs. (1) and (2) to derive expressions for imaging resolution in the case of uniform illumination. However, these expressions overpredict the resolving power of the actual system since Gaussian beams are propagated by single-mode fibers, rather than uniform illumination. For non-uniform illumination, taking into account truncated Gaussian beams, the detector power given by Eq. (7) may be numerically solved as a function of axial (z_d) and transverse displacements (x_d and y_d), with the aid of the PSFs expressed in Eqs. (3) and (4). The integrals are evaluated in Matlab, using the 99%-transmission weighting function given in Eq. (5). A symmetric setup is

assumed (identical illumination and collection optics) with $n \sim 1.4$, $\alpha = \alpha_i = \alpha_c = 0.21$ rad, $\theta = 30^\circ$, and $\lambda = 1.31 \mu\text{m}$ (see Section 3.1 for details). In Fig. 2(a), the theoretical axial response is plotted for the dual-axes system, along with an axial response for a single-axis confocal with an identical -3 dB (FWHM) axial resolution of $4.15 \mu\text{m}$. The main lobe of the single-axis response falls off as $1/z^2$ whereas the dual-axes response falls off as a Gaussian as $\exp(-kz^2)$, offering superior dynamic range and rejection of out-of-focus scattered light. A numerically simulated transverse response, for the same dual-axes system, is shown in Fig. 2(b).

The truncated Gaussian illumination model, which realistically models the fiber-optic-coupled system used, gives theoretical FWHM resolutions of $\Delta x_d = 2.41 \mu\text{m}$, $\Delta y_d = 2.09 \mu\text{m}$, and $\Delta z_d = 4.15 \mu\text{m}$ [Figs. 2(a) and 2(b)].

Finally, a simple expression for the dual-axes resolution may be calculated for full (untruncated) Gaussian beams by analytically solving the diffraction integral given in Eqs. (3) and (4). In the absence of an aperture, the integrals in Eqs. (3) and (4) are now carried out to infinity:²³

$$U_i(v_i) \propto \int_0^\infty \rho e^{-\left(\frac{\pi\rho}{2}\right)^2} J_0(\rho v_i) d\rho = \frac{2}{\pi^2} \exp\left(-\frac{v_i^2}{\pi^2}\right). \quad (10)$$

The collection PSF, $U_c(v_c)$, is analogous. These calculations are performed for a point reflector at the focal plane ($u_i=u_c=0$) with the 99% Gaussian weighting function given earlier in Eq. (5). Substituting Eq. (2) yields

$$U_i(v_i) \propto \exp\left[-\frac{4n^2\alpha_i^2}{\lambda_i^2}(x_i^2 + y_i^2)\right], \quad (11)$$

where the small-angle assumption is made that $\sin \alpha_i = \alpha_i$. Note that α_i refers to the beam half-angle referenced to the lens aperture, or in this case, the 99% power-transmission half-angle of the Gaussian beams.

The coordinate transformations of Eq. (1) may be used, along with Eq. (11), to solve for the detector signal, Eq. (7). For the transverse response at the focal plane ($z_d=0$), the signal may be written as

$$V_d = A \exp\left[-\frac{8n^2\alpha_i^2}{\lambda_i^2}(x_d^2 \cos^2 \theta + y_d^2)\right] \cdot \exp\left[-\frac{8n^2\alpha_c^2}{\lambda_c^2}(x_d^2 \cos^2 \theta + y_d^2)\right]. \quad (12)$$

Similarly, for the axial response, we assume $x_d=y_d=0$ so that

$$V_d = A \exp\left[-8n^2 z_d^2 \sin^2 \theta \left(\frac{\alpha_i^2}{\lambda_i^2} + \frac{\alpha_c^2}{\lambda_c^2}\right)\right]. \quad (13)$$

For a symmetric dual-axes reflectance confocal, $\alpha_i = \alpha_c$ and $\lambda_i = \lambda_c$. The FWHM resolutions may be calculated from Eq. (12) and (13):

$$\Delta x_d = \frac{0.416\lambda}{n\alpha \cos \theta} \quad \Delta y_d = \frac{0.416\lambda}{n\alpha} \quad \Delta z_d = \frac{0.416\lambda}{n\alpha \sin \theta}. \quad (14)$$

For the prototype used in this study, Eq. (14) yields a theoretical resolution (FWHM) of $\Delta x_d = 2.14 \mu\text{m}$, $\Delta y_d = 1.85 \mu\text{m}$,

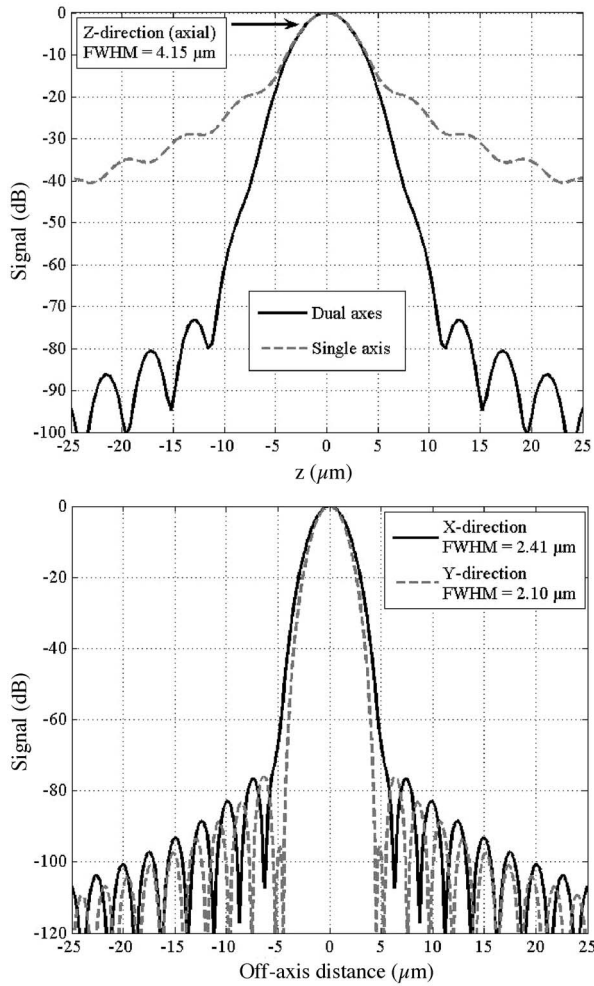


Fig. 2 (a) Theoretical axial response (z_d) to a point reflector for a dual-axes and single-axis confocal with equivalent -3 -dB (FWHM) axial resolutions of $4.15 \mu\text{m}$. Gaussian beams are assumed, truncated to allow 99% power transmission. Dual-axes specifications: $n=1.4$; $\alpha=0.21 \text{ rad}$, $\theta=30^\circ$, $\lambda=1.3 \mu\text{m}$. The single-axis NA=0.58. The main lobe of the single-axis response falls off as $1/z^2$, whereas the dual-axes response falls off as $\exp(-kz^2)$, as expressed in Eq. (13), offering superior scattering rejection and dynamic range. (b) Theoretical transverse response (x_d and y_d) to a point reflector for a dual-axes confocal. Dual-axes specifications are identical to the system analyzed in part (a) (using truncated Gaussian beams). Simulated -3 -dB (FWHM) resolutions are 2.41 and $2.10 \mu\text{m}$, for the x_d and y_d directions, respectively.

and $\Delta z_d=3.71 \mu\text{m}$ for untruncated Gaussian beams. Note that these FWHM values differ significantly, by about 12%, from the truncated Gaussian beam simulations shown in Figs. 2(a) and 2(b). This results from the fact that significant diffraction effects exist even though a large aperture is used to allow 99% power transmission of our Gaussian beams.²¹ The most accurate value for the theoretical resolution of our dual-axes confocal, with Gaussian beams truncated to allow 99% power transmission, was therefore numerically derived and shown in Figs. 2(a) and 2(b). An empirical expression, for convenient use in calculations, is Eq. (14) increased by 12%:

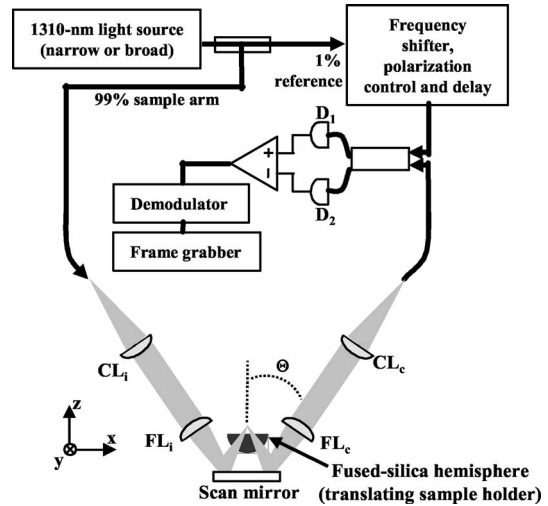


Fig. 3 Optical and electronic circuit for the dual-axes confocal reflectance microscope.

$$\Delta x_d = \frac{0.466\lambda}{n\alpha \cos \theta} \quad \Delta y_d = \frac{0.466\lambda}{n\alpha} \quad \Delta z_d = \frac{0.466\lambda}{n\alpha \sin \theta}. \quad (15)$$

3 Materials and Methods

3.1 Optical Design

Previously, we demonstrated a dual-axes confocal reflectance microscope to distinguish squamous from glandular mucosa in the setting of Barrett’s esophagus.¹¹ In that system, a broadband light source provided a low-coherence gate to suppress the large spatial side lobes (diffraction fringes) due to heavily truncated beams. The current system, with less Gaussian beam truncation (99% power transmission), reduces side-lobe levels for improved performance with a narrowband light source and no coherence gate. In addition, the increased power transmission makes the system more optically efficient. Figure 3 illustrates the optical circuit. The focusing lenses, FL_i and FL_c , have been replaced by microscope objectives (Nikon EPI SLWD 10x) to increase the NA from 0.16 to 0.21, resulting in a resolution of $<5 \mu\text{m}$ to achieve subcellular imaging. Also, optimized collimating lenses, CL_i and CL_c , are employed (Lightpath GPX-10-30) so that the beams are truncated by FL_i and FL_c to allow 99% power throughput.

Finally, we have modified the microscope stage so that the tissue sits on a fused-silica hemisphere, providing several advantages:

1. The curved surface of the hemisphere provides a normal interface to minimize off-axis aberrations, due to coma and astigmatism, as the beams cross the air-to-glass boundary.
2. The wave-front curvature of the focused beams is matched to the curved surface of the hemisphere, minimizing spherical aberrations that would result from focusing a beam through a flat interface from one index to another. Note that small aberrations will still occur during scanning when the beams are out of their neutral positions.
3. Since the refractive index of fused silica ($n=1.45$) is similar to the index of the tissue samples, the beams are

index-matched to minimize aberrations as they enter into the tissue specimen that rests on the flat surface of the hemisphere.

4. The effective NA of the beams is increased. Normally, if a beam is being focused from air into a higher-index material, the NA is preserved due to Snell's law. However, the curved surface of the hemisphere, when well-aligned, preserves the half-angle of the focused beams, thereby increasing the NA by n (1.45 for fused silica).

5. The hemisphere serves as a translating sample holder, which is vertically translated as the slow axis in the raster scan.

One feature of note for the hemisphere is that the curved surface affects the trajectory of the beams as they are scanned. The hemisphere acts to demagnify the scanning range of the beams, to first order, by $1/n$.²⁴ For example, a 250- μm axial translation of the stage causes the beams to scan 150 μm within the sample. Similarly, lateral translations are demagnified by roughly $1/n$. These effects have been validated by ray-tracing simulations (Zemax). All image dimensions presented in this study have been experimentally measured and calibrated.

The space-efficient hemispherical scanning stage enables larger deflections, and therefore a larger scan range, to be made by the galvanometric scan mirror and the piezoelectric vertical translation stage. This eliminates stitching artifacts from having to tile smaller images. The full deflection of the scan mirror (GSI Lumonics VM500) and a 1-mm piezo stage (Physik Instrumente P-290) are used to achieve a field of view within the sample of 610 μm by 640 μm (vertical by horizontal). The mirror is scanned with a sinusoid waveform at 750 Hz (fast axis), and the piezo stage is scanned with a sawtooth waveform at 1 Hz (slow axis). A frame-grabber pixel rate of 1.275 MHz is utilized to acquire images that are 725 pixels high by 750 pixels wide at one frame per second.

Balanced heterodyne detection is accomplished by using an acousto-optic modulator to frequency-shift the 1% reference arm radiation by 55 MHz. A beat signal at this frequency is produced by a fiber Mach-Zehnder interferometer (Newport 50/50 fiber coupler). The interferometer mixes the radiation collected from the sample arm with that from the reference arm. When a broadband light source is used (AFC Technologies Inc. BBS1310B-TS), it is necessary to match the path lengths of the reference and sample arms to within the coherence length of the source ($\sim 50 \mu\text{m}$). A polarization controller in the reference arm also helps to maximize the heterodyne signal and contrast. The 55-MHz carrier signal, detected with an InGaAs balanced receiver (New Focus), is demodulated with a spectrum analyzer at a video bandwidth of 3 MHz. The log-compressed output is fed into an 8-bit frame grabber, digitized, and displayed at one frame per second. The narrowband light source, which was preferentially used in this study, is a diode-pumped nonplanar ring oscillator laser at 1319 nm (JDS Uniphase, formerly Lightwave Electronics 125-1319-100). The line width of this laser is $< 5 \text{ kHz}$, corresponding to a coherence length of over 50 km. Imaging at 1.3 μm enables deep-tissue penetration, is a convenient telecom region where fiber-optic components are readily available at low cost, and is a wavelength that has been well utilized in previous studies.¹³⁻¹⁵

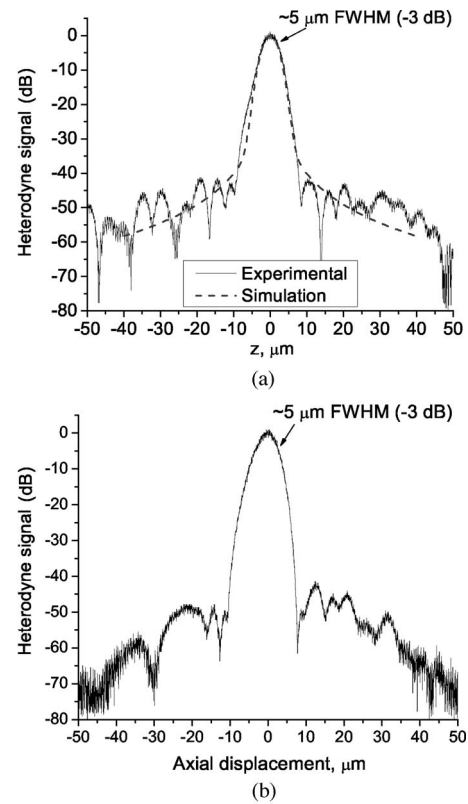


Fig. 4 (a) Axial (z -direction) response to a plane reflector using a narrowband laser source and no coherence gate. The dashed curve represents the simulated response to a plane reflector, calculated using diffraction theory. (b) Axial (z -direction) response to an air-glass interface using a broadband light source to provide a low-coherence gate.

Optical heterodyning is a well-established technique in laser-scanning microscopy.²⁵ Coherent detection at a precise heterodyne frequency (55 MHz in this case) provides optical amplification in order to overcome detector noise to reach the shot-noise limit and to improve image contrast deep within scattering media (several mean-free paths) for single-axis confocal microscopes.²⁶ The assumed reason for this improvement is that the detection is limited by a diminutive signal from loss of light, so that detector noise dominates, rather than background noise from scattered light. This is even more true in dual-axes confocal microscopy, which exhibits improved rejection of scattered light [Fig. 2(a)], albeit at the cost of low-NA collection (lower signal). Therefore, coherent optical amplification is utilized to obtain the sensitivity described in Section 4.1 and to image with deep-tissue penetration, especially at the fast frame rates and short-pixel dwell times desired. Photomultiplier tubes (PMTs), which exhibit low dark counts and noise-free gain, are a possible alternative to heterodyne detection. PMTs at 1319 nm are available but are currently too expensive to consider for use at this wavelength.

3.2 Tissue Samples and Preparation

Informed consent was obtained from all patients in this study, approved by the Institutional Review Board (IRB) of the Stanford University School of Medicine. Fresh biopsy speci-

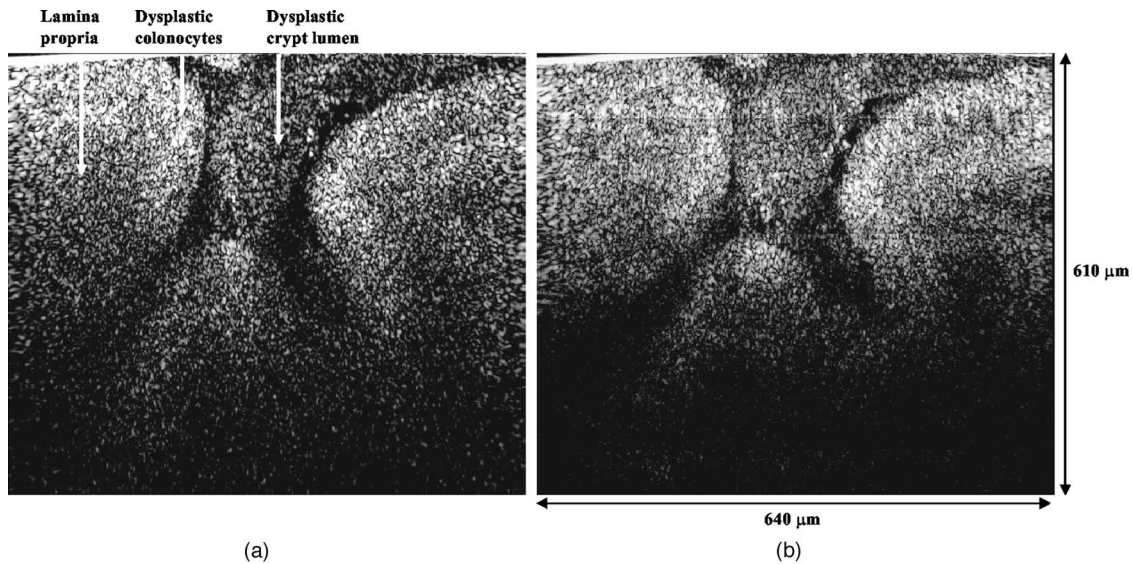


Fig. 5 (a) Vertical section image of an adenomatous polyp using a narrowband laser source. See text for details. (b) Vertical section image of an adenomatous polyp using a broadband light source. See text for details.

mens were collected by pinch biopsy during routine colonoscopy, stored in a saline solution, and placed on ice. The specimens were then imaged within an hour of resection. Immediately prior to imaging, 5% acetic acid was applied topically to improve contrast. After image collection, the specimens were fixed in formalin and submitted for routine histology (H&E). Five to ten specimens each, of normal mucosa, hyperplastic polyps, and adenomatous polyps, were obtained from 15 patients.

4 Results and Discussion

4.1 System Characterization

A plane mirror is used to measure the axial response of the system. A reflecting edge is also used to measure the transverse response. An axial resolution of $5\ \mu\text{m}$ and a transverse resolution of $4\ \mu\text{m}$ (FWHM) is measured, comparing well with the theoretical diffraction-limited results calculated in Section 2. The system sensitivity is measured by attenuating a known intensity of reflected light collected from an air-glass interface until unit SNR is achieved. At a measurement bandwidth of 3 MHz, the minimum detectable signal intensity is approximately 2 pW. The maximum intensity of light incident on the sample is approximately 20 mW. By defining “sensitivity” as the ratio of these two values, a sensitivity of 100 dB is calculated, a comparable figure to that achieved by OCT. In practice, the dynamic range is reduced by optical-coupling losses, as well as by sample absorption and scattering.

4.2 Narrowband vs. Broadband Performance

The axial response of the dual-axes system to reflection from the flat surface (glass-air interface) of the hemispherical sample holder was measured. Figures 4(a) and 4(b) plot the narrowband and broadband responses, respectively, as a function of axial (z_d) displacement. In Fig. 4(a), a simulated response is also shown, calculated (in Matlab) using diffraction

theory by integrating Eq. (7) over the entire x - y plane to model a plane reflector. The reduced noise floor (~ 80 dB) in the wings of the plot shown in Fig. 4(b) suggests that the coherence gate additionally reduces the collection of out-of-focus scattered light. However, for both the narrowband and broadband systems, signal from scattered light within $\pm 25\ \mu\text{m}$ of the focal plane is the dominant noise source, resulting in similar image quality. The use of a broader-band light source may improve the ability of the coherence gate to reject out-of-plane scattered light, but at greater cost and design complexity.

The vertical sections, shown in Figs. 5(a) and 5(b), are taken from a premalignant (adenomatous) polyp. These figures demonstrate the comparable image quality obtained with a narrowband or broadband source (low-coherence gate). The broadband system introduces the additional complexity of having to adjust the delay stage in order to match the reference and sample arm lengths through a full vertical scan. Although translating the sample holder does not alter the physical path length of the sample arm during vertical scanning, focusing the beams deeper into tissue increases the effective path length of the sample arm due to the higher index of tissue compared to air. Therefore, a large vertical scan requires an adjustment of the delay stage. This was done manually in this system, resulting in the slight tiling artifacts in Fig. 5(b).

All subsequent images presented in this article were obtained without a coherence gate using a narrowband source.

4.3 Images of Colonic Mucosa

As shown in Fig. 6(a), normal colonic mucosa reveals regularly spaced crypts extending vertically in the plane perpendicular to the mucosal surface. Horizontal (*en face*) images were rendered in software (Amira 3.0) after acquiring many vertical sections at $5\text{-}\mu\text{m}$ increments. Note that the horizontal renderings are under-resolved in one direction since the vertical slices used to reconstruct the horizontal image are ob-

tained at 5- μm increments, whereas proper sampling in fulfillment of the Nyquist criteria would require 2- μm increments (transverse resolution is 4 μm). Figure 6(b) displays a horizontal rendering, at 150 μm beneath the tissue surface, of 80 vertical image slices of normal mucosa. In this horizontal section, a high-intensity ring is observed that can be localized to the nuclei of the colonocytes populating the basal periphery of the crypts. The corresponding histology is shown in Fig. 6(c). The crypts are fairly circular in appearance and are uniformly separated with goblet cells (clear, mucin-filled vacuoles) surrounding the crypt lumen.

In respective order, Figs. 7(a)–7(c) show a vertical section, a rendered horizontal section, and the corresponding histology from a biopsy specimen of a hyperplastic (benign) polyp. Excess cytoplasmic mucin in the colonocytes gives the characteristic appearance of an undulating “star-shaped” pattern in the luminal cross-section of the hyperplastic crypts.

A vertical section of an adenomatous polyp is shown in Fig. 8(a). Significant contrast is visible between the colonocytes lining the crypt lumen and the lamina propria. This contrast is evident in the rendered horizontal sections shown in Figs. 8(b) and 8(c), taken from two different adenomatous polyp biopsies. In dysplastic colonic mucosa, the diameter of the crypts is increased, as is the size of the colonocytes lining the crypt lumen. Furthermore, the crypts are morphologically distorted, lacking a consistently-circular cross-sectional shape and appearing more elliptical in cross-section. The nuclei are “atypical,” in that nuclei are larger and more stratified, making for a thickened nuclear layer in the epithelium lining the colonic crypts, as seen in Fig. 8(d). These nuclear features, along with irregularities in the crypt architecture, are characteristic of dysplasia. Thick bright rings are seen in Figs. 8(a)–8(c), likely caused by increased scattering from enlarged nuclei. The increased light-scattering properties of dysplastic nuclei have been confirmed in other studies.²⁷

For preliminary quantitative image comparison, the contrast-to-noise ratio (CNR) is defined as

$$\text{CNR} \equiv \frac{I - I_{\text{lumen}}}{\sigma_{\text{lumen}}} \quad (16)$$

This figure of merit accounts for different gain settings between images by normalizing with a background noise term (σ_{lumen} , here defined as the standard deviation in the pixel intensities of the crypt lumen). I and I_{lumen} are the average intensities of the pixels within a chosen region of interest in our raw images. For all noise and intensity calculations, square regions are chosen that are 20 by 20 pixels in dimension. Figure 9 plots the CNR for both the highly scattering nuclei as well as the lamina propria, in normal, hyperplastic, and dysplastic (adenomatous) mucosa. In each case, the CNR from 10 representative image regions are averaged to obtain the values plotted in Fig. 9. Compared to benign mucosa (normal and hyperplastic), the nuclear CNR is significantly higher for dysplastic mucosa, as expected due to nuclear atypia. The CNR of the lamina propria is slightly increased for hyperplasia, compared to normal mucosa, perhaps suggesting that excess cytoplasm in the colonocytes not only leads to a characteristic “star-shaped” luminal morphology, but also compresses the surrounding lamina propria, thereby leading to increased scatter in the denser tissue. This increased scatter in

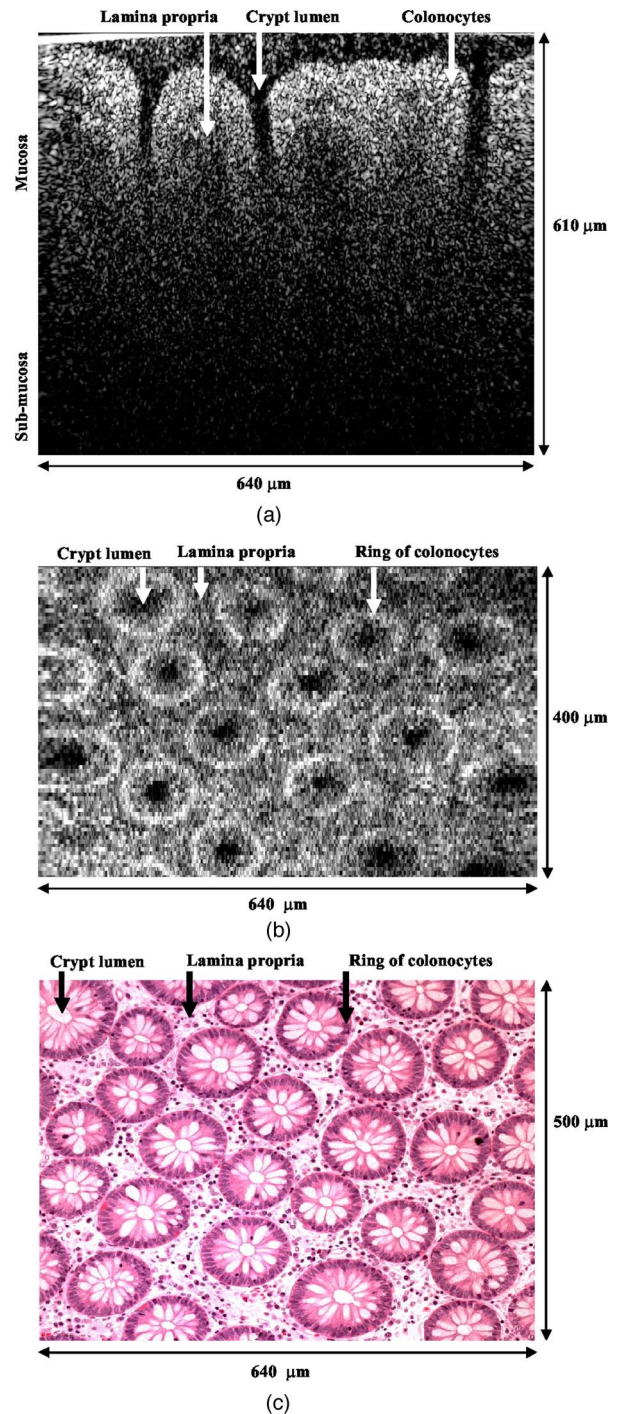


Fig. 6 (a) Vertical section image of normal colonic mucosa, showing vertical crypt channels. (b) A horizontal section image 150 microns beneath the mucosal surface of a normal colonic biopsy, rendered from 80 vertical sections. (c) A horizontal histological image (H&E staining) of normal colonic mucosa.

the lamina propria is further apparent in dysplastic mucosa.

An advantage of this intravital microscope, as well as future *in vivo* devices, is that tissue samples may be more reliably oriented with respect to the imaging axes than histological samples are on a slide. This allows for accurate quantification of morphological dimensions. Here we measure

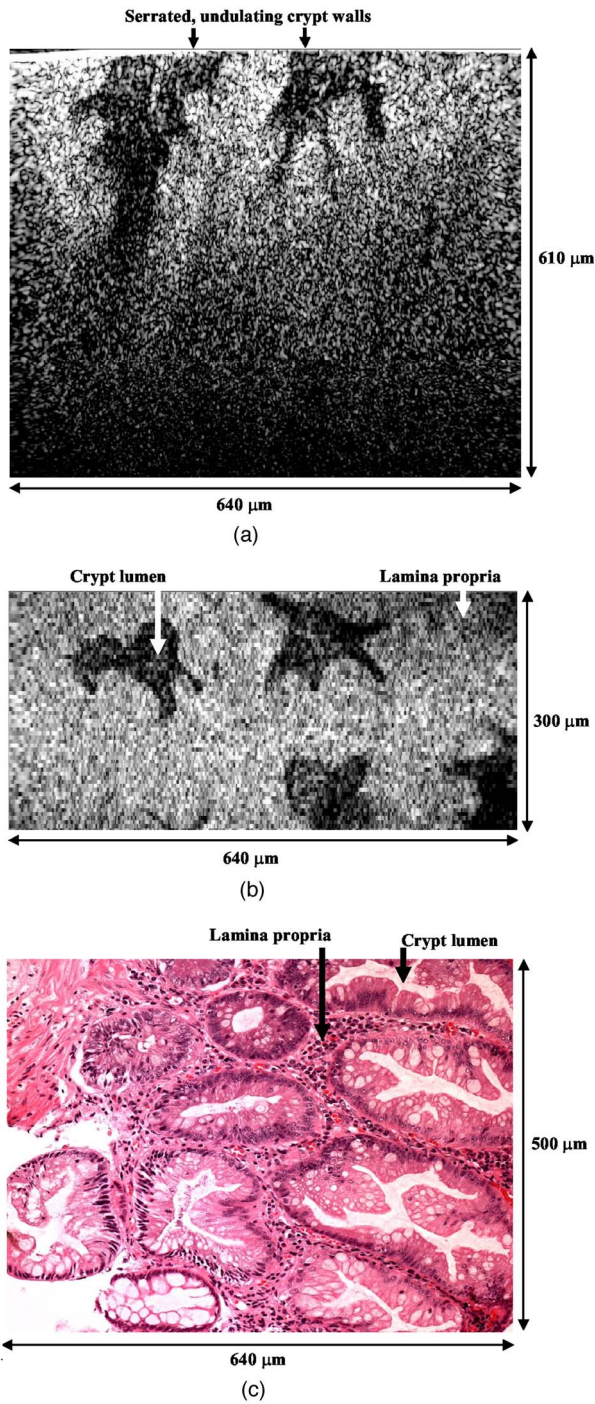


Fig. 7 (a) Vertical section image of mucosa from a hyperplastic polyp. (b) Horizontal section image 75 microns beneath the mucosal surface of a hyperplastic polyp, rendered from 60 vertical sections. (c) Histology (H&E staining) of the hyperplastic polyp imaged in parts (a) and (b).

the eccentricity of the crypts, for horizontally rendered images of normal and dysplastic mucosa. We define the eccentricity as the ratio between the longest dimension of the crypts (measured to the basal end of the colonocytes) and the dimension along the perpendicular bisector of this long axis. The results plotted in Fig. 10, for 10 representative crypts from normal

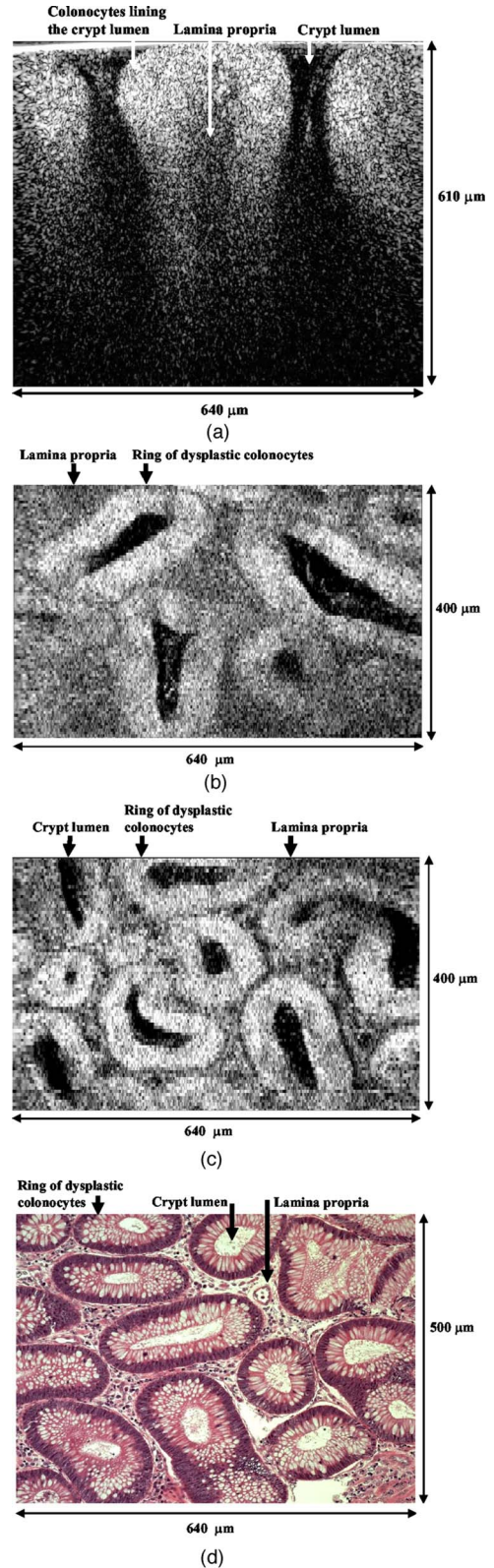


Fig. 8 Vertical section image of mucosa from an adenomatous (dysplastic) polyp, showing a large crypt channel lined by a thick layer of highly scattering colonocytes. (b) Horizontal section 125 microns beneath the mucosal surface of the adenomatous polyp shown in part (a), rendered from 80 vertical sections. (c) Horizontal section image 100 microns beneath the mucosal surface of an adenomatous polyp, rendered from 80 vertical sections. (d) Histology (H&E staining) of an adenomatous polyp.

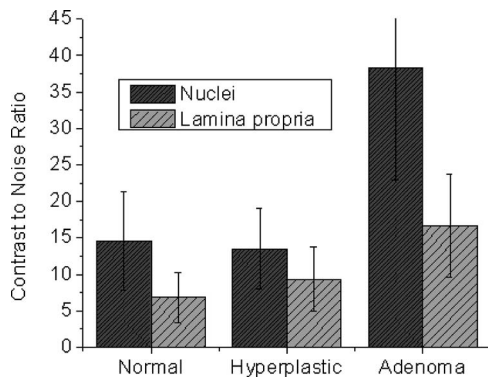


Fig. 9 Average contrast-to-noise ratios (of the nuclei and lamina propria) for normal, hyperplastic, and dysplastic (adenomatous) mucosa. Error bars indicate the standard deviation.

and dysplastic mucosa, show a large variation and high degree of eccentricity in adenomatous crypts, consistent with the images shown earlier.

4.4 Future In Vivo Imaging

The purpose of this study is to demonstrate, on a tabletop prototype, the diagnostic utility of a dual-axes confocal imaging system with the potential for miniaturization and *in vivo* use. A 10-mm-diameter hand-held version of this microscope is currently being assembled and tested for dermatological applications. A similar version with a 5-mm diameter is also being designed for *in vivo* imaging of the colon through a therapeutical colonoscope with a large instrument channel. These miniature designs will incorporate a 2D scanning MEMS mirror actuated with electrostatic comb drives.²⁸ Horizontal (*en face*) images will be obtained by scanning the illumination and collection beams in tandem. These devices will also possess the ability to image at a variety of depths through either manual or motorized vertical actuation. In addition to their miniature size, one benefit of these MEMS mirrors is their ability to scan at high speeds in both the *x*- and *y*-directions, enabling fast frame rates for *en face* imaging. For example, the resonant frequency of the fast axis, at around 3 kHz, will easily enable imaging rates of many frames per second. Details of the miniature design, as well as the imaging performance of the device, are beyond the scope of this article but will be presented in a future publication. Light sources in addition to 1.3 μm will be employed in future devices, for improved resolution as well as the ability to perform fluorescence imaging with targeted fluorophores.¹⁸

5 Conclusions

In this article, diffraction theory is used to model dual-axes confocal response and resolution, demonstrating good agreement with experimental results. A simple expression for transverse and axial resolution is derived for illumination with truncated Gaussian beams, as is relevant to a fiber-optic-coupled system. Off-axis collection, without a coherence gate, is sufficient to spatially filter out-of-focus light for imaging large vertical sections with high contrast and deep-tissue penetration. The use of a narrowband source simplifies the microscope design, reduces cost, and allows for collection of inco-

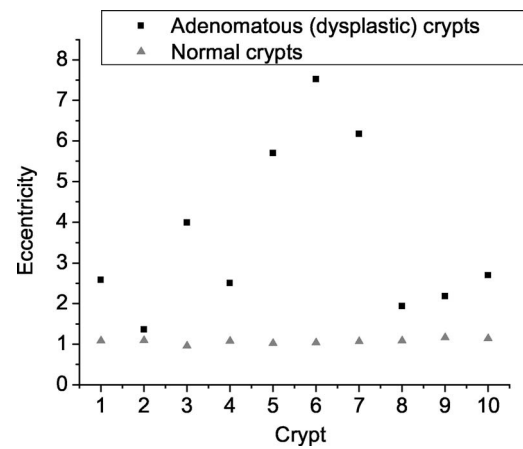


Fig. 10 Eccentricity measurements of normal and adenomatous colonic crypts ($n=10$) imaged with the dual-axes confocal reflectance microscope.

herent light such as fluorescence. The use of optimized low-NA optics ($NA = 0.21$), Gaussian beam truncation (99% truncation), and an index-matching hemispherical sample holder allows for collection of vertical cross-sectional images with 5- μm axial and 4- μm lateral resolution over a field of view of 610 μm (deep) by 640 μm (wide) at one frame per second.

We show that a dual-axes confocal reflectance microscope using a narrowband light source at 1310 nm can distinguish among normal, hyperplastic, and dysplastic (precancerous) colonic mucosa *ex vivo*. Clear differences in glandular crypt size, eccentricity, and contrast are apparent and quantifiable in the dual-axes reflectance confocal images. These results illustrate the diagnostic potential of a future miniature endoscope-compatible instrument that we are developing for *in vivo* imaging. A real-time *in vivo* microscope with optical-sectioning capabilities would provide a powerful tool for improving the speed and accuracy of endoscopic examinations. In addition, such a device could be used for image-guided resection, delineating tumor margins, identifying sub-epithelial lesions, and detecting submucosal invasion.

Acknowledgments

The authors would like to acknowledge funding support from the National Cancer Institute (NCI), through the 5U54 CA105296 Network for Translational Research in Optical Imaging (NTROI), and an NSF Center for Biophotonics Science and Technology (CBST) developmental award. Jonathan Liu is supported by a Canary Foundation/American Cancer Society post-doctoral fellowship for the early detection of cancer. Thomas Wang is supported by the National Institute of Diabetes and Digestive and Kidney Diseases (NIDDK) on Grant number K08 CA096752.

References

1. J. Pawley, Ed., *Handbook of Biological Confocal Microscopy*, 3rd ed., Plenum, New York (1996).
2. G. D. Papworth, P. M. Delaney, L. J. Bussau, L. T. Vo, and R. G. King, "In vivo fibre optic confocal imaging of microvasculature and nerves in the rat vas deferens and colon," *J. Anat.* **192**, 489–495 (1998).

3. Y. S. Sabharwal, A. R. Rouse, L. Donaldson, M. F. Hopkins, and A. F. Gmitro, "Slit-scanning confocal microendoscope for high-resolution *in vivo* imaging," *Appl. Opt.* **38**, 7133–7144 (1999).
4. C. Liang, K. Sung, R. R. Richards-Kortum, and M. R. Descour, "Design of a high-numerical aperture miniature microscope objective for an endoscopic fiber confocal reflectance microscope," *Appl. Opt.* **41**, 4603–4610 (2002).
5. D. L. Dickensheets and G. S. Kino, "Silicon-micromachined scanning confocal optical microscope," *J. Microelectromech. Syst.* **7**, 38–47 (1998).
6. R. Kiesslich, J. Burg, and M. Vieth, "Confocal laser endoscopy for diagnosing intraepithelial neoplasias and colorectal cancer *in vivo*," *Gastroenterology* **127**, 706–713 (2004).
7. E. Laemmel, M. Genet, G. Le Goualher, A. Perchant, J. F. Le Gargasson, and E. Vicaud, "Fibered confocal fluorescence microscopy (Cell-viZio) facilitates extended imaging in the field of microcirculation. A comparison with intravital microscopy," *J. Vasc. Res.* **41**, 400–411 (2004).
8. E. H. Stelzer, S. Lindek, S. Albrecht, R. Pick, G. Ritter, N. Salmon, and R. Stricker, "A new tool for the observation of embryos and other large specimens: Confocal theta fluorescence microscopy," *J. Microsc.* **179**, 1–10 (1995).
9. S. Lindek and E. H. K. Stelzer, "Optical transfer functions for confocal theta fluorescence microscopy," *J. Opt. Soc. Am. A* **13**, 479–482 (1996).
10. R. H. Webb and F. Rogomentich, "Confocal microscope with large field and working distance," *Appl. Opt.* **38**, 4870–4875 (1999).
11. T. D. Wang, M. J. Mandella, C. H. Contag, N. Y. Chan, and G. S. Kino, "Dual axes confocal microscope with post-objective scanning and low coherence heterodyne detection," *Opt. Lett.* **28**, 1915–1917 (2003).
12. D. Huang, E. A. Swanson, C. P. Lin, J. S. Schuman, W. G. Stinson, W. Chang, M. R. Hee, T. Flotte, K. Gregory, C. A. Puliafito, and J. G. Fujimoto, "Optical coherence tomography," *Science* **254**, 1178–1181 (1991).
13. B. E. Bouma and G. J. Tearney, Eds., *Handbook of Optical Coherence Tomography*, Marcel Dekker, New York (2002).
14. A. M. Rollins, R. Ung-arunyawee, A. Chak, R. C. K. Wong, K. Kobayashi, M. V. Sivak Jr., and J. A. Izatt, "Real-time *in vivo* imaging of human gastrointestinal ultrastructure by use of endoscopic optical coherence tomography with a novel efficient interferometer design," *Opt. Lett.* **24**, 1358–1360 (1999).
15. P. Hsiung, L. Pantanowitz, A. D. Aguirre, Y. Chen, D. Phatak, T. H. Ko, S. Bourquin, S. J. Schmitt, S. Raza, J. L. Connolly, H. Mahimo, and J. G. Fujimoto, "Ultrahigh-resolution and 3-dimensional optical coherence tomography *ex vivo* imaging of the large and small intestines," *Gastrointest. Endosc.* **62**, 561–574 (2005).
16. J. A. Izatt, M. R. Hee, G. M. Owen, E. A. Swanson, and J. G. Fujimoto, "Optical coherence microscopy in scattering media," *Opt. Lett.* **19**, 590–592 (1994).
17. A. Aguirre, P. Hsiung, T. H. Ko, I. Hartl, and J. G. Fujimoto, "High-resolution optical coherence microscopy for high-speed, *in vivo* cellular imaging," *Opt. Lett.* **28**, 2064–2066 (2003).
18. T. D. Wang, C. H. Contag, M. J. Mandella, N. Y. Chan, and G. S. Kino, "Confocal fluorescence microscope with dual-axis architecture and biaxial postobjective scanning," *J. Biomed. Opt.* **9**, 735–742 (2004).
19. K. Kelly, H. Alencar, M. Funovics, U. Mahmood, and R. Weissleder, "Detection of invasive colon cancer using a novel, targeted, library-derived fluorescent peptide," *Cancer Res.* **64**, 6247–6251 (2004).
20. M. Born and E. Wolf, *Principles of Optics*, 7th ed., Cambridge Press, Cambridge, U. K. (1999).
21. A. E. Siegman, *Lasers*, University Science Books, Mill Valley, CA (1986).
22. T. D. Wang, M. J. Mandella, C. H. Contag, and G. S. Kino, "Dual axes confocal microscope for high-resolution *in vivo* imaging," *Opt. Lett.* **28**, 414–416 (2003).
23. I. S. Gradshteyn and I. M. Ryzhik, *Table of Integrals, Series, and Products*, 6th ed., edited by A. Jeffrey and D. Zwillinger, Eds., Academic Press, San Diego (2000).
24. S. M. Mansfield and G. S. Kino, "Solid immersion microscope," *Appl. Phys. Lett.* **57**, 2615–2616 (1990).
25. T. Satawari, "Optical heterodyne scanning microscope," *Appl. Opt.* **12**, 2768–2772 (1973).
26. M. Kempe, W. Rudolph, and E. Welsch, "Comparative study of confocal and heterodyne microscopy for imaging through scattering media," *J. Opt. Soc. Am. A* **13**, 46–52 (1996).
27. R. Drezek, M. Guillaud, T. Collier, I. Boiko, A. Malpica, C. Macaulay, M. Follen, and R. Richards-Kortum, "Light scattering from cervical cells throughout neoplastic progression: Influence of nuclear morphology, DNA content, and chromatin texture," *J. Biomed. Opt.* **8**, 7–16 (2003).
28. H. Ra, Y. Taguchi, D. Lee, W. Piyawattanametha, and O. Solgaard, "Two-dimensional MEMS scanner for dual-axes confocal *in vivo* microscopy," Tech. Digest of IEEE International Conf. Micro Electro Mechanical Systems, Turkey, Jan. 22–26, 2006, pp. 862–865.